Journal of Power Sources 615 (2024) 235076

Contents lists available at ScienceDirect

Journal of Power Sources

journal homepage: www.elsevier.com/locate/jpowsour

Investigation of calendar ageing of lithium-ion battery through physical models with ex-situ validation

Gabriele Sordi [a,b,c,*], Daniel Luder [b,c], Weihan Li [b,c], Dirk Uwe Sauer [b,c,d], Andrea Casalegno [a], Claudio Rabissi [a]

[a] Politecnico di Milano, Department of Energy, Via Lambruschini 4, 20156, Milano, Italy
[b] Chair for Electrochemical Energy Conversion and Storage Systems, Institute for Power Electronics and Electrical Drives (ISEA), RWTH Aachen University, 52074, Aachen, Germany
[c] Center for Ageing, Reliability and Lifetime Prediction of Electrochemical and Power Electronic Systems (CARL), RWTH Aachen University, 52074, Aachen, Germany
[d] Helmholtz Institute Münster (HI MS), Forschungszentrum Jülich, Jülich, Germany

HIGHLIGHTS

- Ageing effect of 3 temperatures and 4 SOC conditions is tested and simulated.
- P2D and qOCP models quantify 7 + 3 selected physical parameters along the ageing test.
- Consistency between discharge test and EIS is forced for physical soundness.
- Temperature and SOC promote loss of lithium inventory and electrolyte conductivity.
- Half-cell, SEM and EDS ex-situ analyses demonstrate the growth of the SEI layer.

GRAPHICAL ABSTRACT

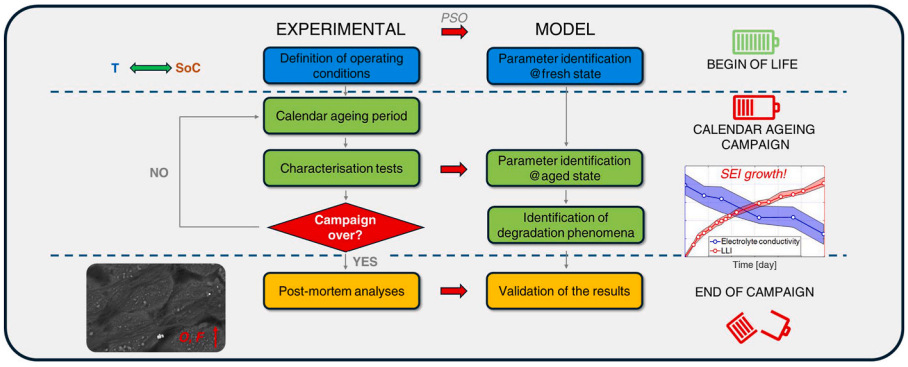

ARTICLE INFO

Keywords:
Lithium-ion batteries
Degradation
Calendar ageing
Model
Ex-situ measurement

ABSTRACT

The estimation of the state of health of a lithium-ion battery is a topic of interest with the spread of battery electric vehicles. According to the desired long lifetime, calendar ageing is a matter of concern due to the known deterioration effect of mid-high environmental temperatures, even during parking periods. In this work, the combined use of an optimised sequence of tests and physical models is applied to investigate degradation due to calendar ageing on a commercial NMC + LMO|Graphite cell type. A calendar ageing campaign on 12 samples is carried out with periodic interruptions for characterisation. This method, already applied to a low-temperature charging campaign, proves its suitability in identifying ageing mechanisms and reproducing the performance of aged cells. SEI layer growth with significant consumption of lithium and electrolyte material is the dominant phenomenon, but mass-transport limitations arise from the positive electrode, too. Physical model parameter identification is challenged with verification measurements like tests on coin cell configuration and microscopies,

* Corresponding author. Politecnico di Milano, Department of Energy, via Lambruschini 4, 20156, Milano, Italy.
E-mail address: gabriele.sordi@polimi.it (G. Sordi).

https://doi.org/10.1016/j.jpowsour.2024.235076
Received 9 May 2024; Received in revised form 30 June 2024; Accepted 15 July 2024
Available online 25 July 2024

resulting in compatibility. This work further verifies the suitability of such a methodology for the degradation of lithium-ion batteries.

1. Introduction

Electric vehicles are spreading worldwide thanks to the advantages of lithium-ion batteries in terms of cost and energy density. Nevertheless, they suffer from capacity loss and resistance rise during their lifetime, which limit their suitability for the automotive sector. Moreover, it is known that degradation occurs even when the battery is not undergoing any load, which is called "calendar ageing".

As a result, the scientific literature is rich in publications dealing with the effect of operating conditions on capacity loss and resistance increase during simple storage. For instance, Keil et al. [1] investigated the capacity loss and resistance increase of lithium-ion batteries of different positive electrode chemistries at three temperatures and sixteen state of charge (SoC) levels. They correlated capacity fade with the potential of the negative electrode, which is responsible for enhancing electrolyte degradation and loss of lithium inventory (LLI). In contrast, no substantial effect of the positive electrode was observed other than in a few extreme conditions. M. Ecker et al. [2] investigated the effect of temperature and voltage during calendar ageing for lithium-nickel-cobalt-manganese-oxide (NMC) cells, verifying Arrhenius's behaviour with temperature and the dominant role of graphite potential. They observed a linear trend of capacity loss, different from Ref. [3], which modelled capacity loss with a square root of time dependence on lithium-iron-phosphate (LFP) batteries. In Ref. [3], the authors investigated the dependence of capacity and resistance over time. They identified an exponential relation with time to the power of 0.75 as the best fit due to the superposition of two ageing phenomena with different time evolution. J. Schmitt et al. [4] studied calendar ageing with electrochemical impedance spectroscopy (EIS) with the aid of an equivalent circuit model (ECM). They related the growth of the series resistance with the reduction of the electrolyte conductivity, but they faced some issues in identifying the source of charge-transfer resistance and diffusion limitations. They assumed a solid electrolyte interphase (SEI)-dominant role on the charge-transfer resistance as consistent with the significant series-resistance increase, namely electrolyte reduction led to an increased SEI layer thickness. However, from pulse tests with different timescales (1s vs 20s), they were able to state that ohmic and charge-transfer losses arise with the same pace of diffusion limitations due to ageing. This latter effect is seldom investigated in the scientific literature. For instance, Stiasny et al. [5] identified diffusional limitations in aged positive electrodes without focusing on this topic to derive a solid interpretation. However, they investigated the ageing of commercial lithium-manganese oxide (LMO) + NMC batteries at 60 °C and high voltage with electrochemical tests and post-mortem analysis, identifying loss of active electrode material (LAM) at the positive electrode and variation of its impedance.

Even though capacity loss and resistance rise are properly investigated, it is quite uncommon to investigate the performance evolution in a wider view. Indeed, although residual capacity and resistance increase are of paramount importance, they are not enough to describe the operation of an aged cell, e.g., overlooking diffusion limitations that might arise. Also, capacity and resistance are seldom the only targets at the modelling level. For instance, Montaru et al. [6] developed a dual-tank model to reproduce the evolution of the open-circuit voltage (OCV) curve of a battery during calendar ageing, exploiting three parameters (electrode capacities and an offset between them) by means of empirical correlations and a physical description of the SEI growth, to get a reasonable prediction of the residual capacity. It also enables the prediction of the evolution of electrode capacities and SEI parasitic current. Li et al. [7] proposed a framework to reproduce the OCV and impedance spectrum during ageing by parameterising a hybrid model with a cuckoo search algorithm. In another work, Zhu et al. [8] implemented the irreversible SEI growth in the pseudo-two-dimensional (P2D) model, which enabled the reproduction of the capacity loss and C/3 charging profiles of some cells aged with calendar ageing at 55 °C at some SoC conditions. However, they focused on understanding the role of the SEI properties rather than simulating the operation of the cells.

However, physical models could provide a more comprehensive description of the battery state, thanks to their physical consistency. Even though it is not very common in scientific publications [9–12], physical models can simulate the operation of the battery under different conditions and loads reliably, also at aged state. By performing the parameter identification for one cell at different ageing states, it is possible to simulate its operation and infer the origin of this effect, e.g. one or more degradation phenomena.

As an example, Zhang et al. [11] exploited the pseudo-two-dimensional (P2D) model with a thermal model in this way. They cycled some cells at 50 °C with constant-current cycles and after a sequence of 20 cycles, they performed two dynamic profiles at two temperature levels as check-up tests. They identified nine important physical parameters by reproducing the check-up data at increasing ageing states and showed how all evidence could be correlated with the solid electrolyte interphase (SEI) growth. They provided very interesting insights, even though the physical origin of some parameter trends remains unclear and they did not perform a validation of the results. Uddin et al. [9] also exploited the P2D model but for a calendar ageing campaign. However, they selected the fitting parameters in agreement with the most likely degradation mechanisms, with the aim of verifying the suitability of the approach rather than applying the tool to investigate the state of health.

Hence, as emerges from the analysis to the best of the authors' knowledge, there are no works in the literature exploiting the P2D model to understand calendar ageing mechanisms, linking them with storage conditions in a physically consistent, holistic approach. Hence, this paper develops and applies a novel methodology, which estimates a high-sensitivity-selected broad set of physical parameters, to a calendar ageing campaign on commercial lithium-ion batteries, performed by combining 12 different storage conditions. Parameter estimation exploits a sensitivity-optimised experimental protocol combining both discharge test and EIS to ensure broad physical consistency of the identified solution. The performance of aged cells is reproduced by periodically solving the parameter identification problem, associating the parameters' evolution with classes of degradation phenomena and to the corresponding battery component.

To avoid biasing the solution and ensure that it is eligible for ageing diagnosis, the several points will be guaranteed:

- The number of fitting parameters should be large enough to simulate the most relevant ageing effects on the performance;
- The selection of fitting parameters should not bias the interpretation of the results, i.e. it should be independent of the ageing conditions;
- The results should be unique and repeatable, considering the uncertainty of experiments and parameter identification method;
- The reliability should be verified, at least for some reference samples, either with additional simulations or tests.

To demonstrate the validity of identified solutions, the model will finally be applied to simulate experimental conditions outside of the training dataset. Also, morpho-chemical ex-situ analyses will be performed and combined with half-cell electrochemical measurements to validate interpretation.

This work aims to investigate calendar ageing on commercial

lithium-ion batteries that underwent calendar ageing. The performance of aged cells is reproduced by solving the parameter identification problem alongside the experimental campaign, and the parameter evolution is associated with classes of degradation phenomena [14].

The outline of this document is as follows. First, the methodology is described in Section 2. Then, Section 3 reports the experimental and modelling results. In Section 4, ex-situ measurements are described, to validate the estimation of some physical parameters.

2. Methodology

The methodology is here summarised, as schematised in Fig. 1. One calendar ageing campaign is conducted under different conditions. Characterisation tests are performed periodically to trace the residual performances. Based on the data collected with characterisation tests, the parameters of the P2D model are identified, exploiting an optimisation algorithm. This procedure is followed progressively along the degradation states, enabling drawing the evolution of the parameters. These trends are then analysed to link them together and associate them with likely degradation phenomena. A description of experimental activities and modelling tools is provided in the following sections. For additional information regarding the methodology, the reader is referred to Ref. [13].

2.1. Experimental sample and testbench

The properties of the samples of the experimental campaigns are listed in Table 1. The positive electrode is a blend of NMC and LMO. All samples were brand-new. Electrolyte and binder compositions are unknown.

The experimental testbench [16] is a custom-developed testing station, including one power supply and two five-channel electronic loads, resulting in eight independent testing channels, each capable of up to 80 A dynamic charge-discharge testing. The system can perform EIS. All tests are performed in a Binder MKF 720 Eucar 6 climatic chamber. Test temperature always refers to the setpoint of the climatic chamber. Sample surface temperature is monitored through type K thermocouples. The calendar ageing campaign is conducted in a Binder KT 53 climatic chamber. For a more detailed description, the reader is referred to Ref. [15].

Table 1
Characteristics of the experimental samples [14].

Property	Value
Manufacturer	SONY
Model	US18650V3
Nominal capacity	2.25 Ah
Voltage cut-offs	2.5V–4.2V
Electrode materials	Graphite/NMC + LMO
Continuous max charge C-rate	1C

2.2. Test matrix

Three calendar ageing campaigns are carried out to investigate the effect of storage conditions on performance fade [3,16]. In particular, twelve cells are aged at controlled conditions, listed in Table 2. The experimental matrix highlights the effect of the SoC and temperature. After 150 days of storage, the campaign at 25 °C is stopped according to the limited extent of degradation. On the contrary, 100 % SoC condition

Table 2
Experimental matrix of the calendar ageing campaign.

Label	Temperature [°C]	SoC [%]	Duration of the campaign [day]
Calendar 25-100	25	100	150
Calendar 25-80	25	80	150
Calendar 25-50	25	50	150
Calendar 25-10	25	10	150
Calendar 45-100	45	100	305
Calendar 45-80	45	80	445
Calendar 45-50	45	50	445
Calendar 45-10	45	10	445
Calendar 60-100	60	100	70
Calendar 60-80	60	80	129
Calendar 60-50	60	50	129
Calendar 60-10	60	10	70

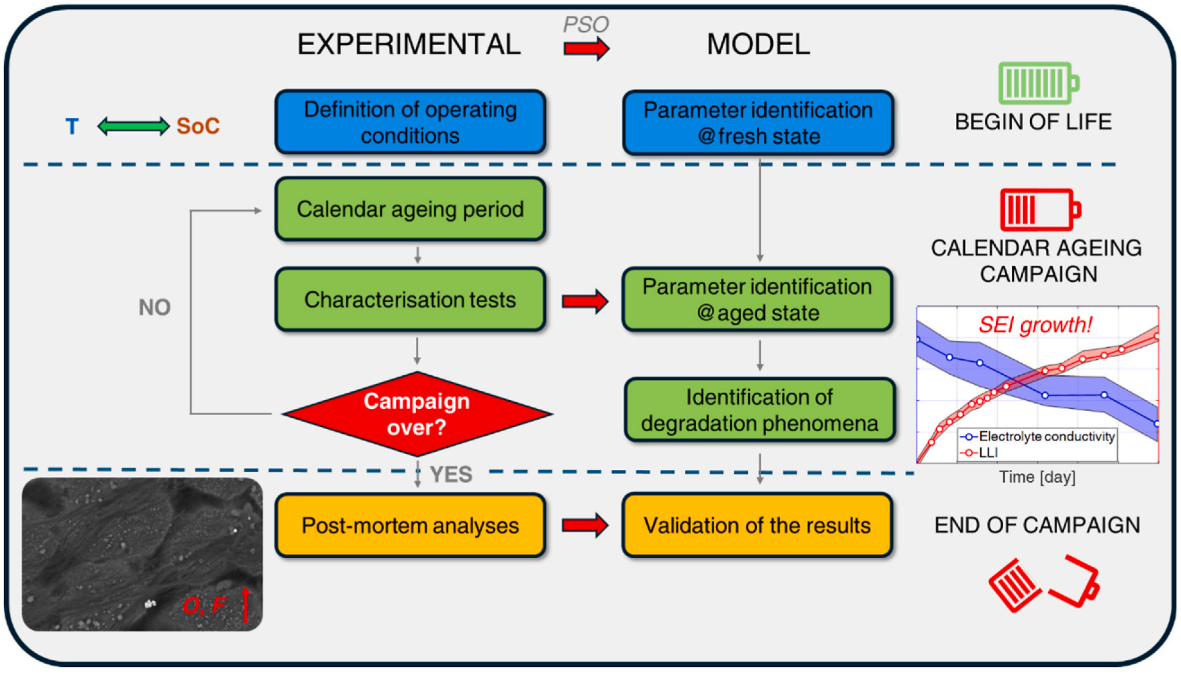

Fig. 1. Logical scheme of the methodology.

at both 45 °C and 60 °C led to severe self-discharge, which forced them to stop their tests earlier than the other SoC conditions. The campaigns are periodically interrupted to perform characterisation tests. Two cells underwent the same storage conditions for repeatability in the 25 °C and 45 °C cases.

2.3. Characterisation procedure

The characterisation procedure includes.

- One full discharge at 25 °C and C/10, considered as quasi-equilibrium condition
- Two partial discharges performed at
  - o 10 °C, 2C, from 100 % to 50 % SoC (discharge D1)
  - o 25 °C, 1C, from 50 % SoC to the lowest voltage cut-off (discharge D2)
- Two EISs performed at
  - o 10 °C, 100 % SoC, with 40 logarithmically-spaced frequencies from 4 kHz to 10 mHz (EIS E1)
  - o 25 °C, 50 % SoC, with 40 logarithmically-spaced frequencies from 4 kHz to 10 mHz (EIS E2)

The full C/10 discharge is exploited to identify thermodynamic losses, while the remaining tests allow for the identification of worsening of kinetic and diffusive properties. These tests are required to identify the physical parameters of the models, described in the next section. The choice of this experimental protocol comes from combining limited testing time with maximising the identifiability of the physical parameters [15].

2.4. Modelling tools

Two physical models are exploited to interpret experimental data, namely an equilibrium model and P2D physical model. Parameters of the two models are identified by means of a particle swarm optimisation (PSO) algorithm, providing the best fit for the experimental data of the tests of the characterisation procedure just described, in a stepwise procedure detailed below [13]. PSO is an evolutionary algorithm with a single objective function, which searches for the best solution to a problem by quantifying the cost function, which is associated with various combinations of parameters values and improving the solution over different iterations [15,17].

The equilibrium model is applied for low C-rate discharges to identify the LLI and loss of active electrode material of the positive and negative electrodes, namely LAMp and LAMn, by reproducing the differential voltage curve at C/10 and 25 °C of the characterisation procedure described in Section 2.3. It includes open-circuit potential curves (OCPs) of the electrodes as look-up tables as input information and overpotentials are simulated with a single lumped resistance. LAMs are implemented as purely delithiated. Stoichiometric operating boundaries of the electrodes are estimated with half cell C/50 cycles in coin cell format for a fresh sample. For an aged cell, these parameters implicitly on the values of LLI and LAM, thus they are not included in the list of fitting parameters. Indeed, a non-linear solver is exploited to match the OCP curves for aged cells, taking into account the values of LAM, which work as contraction factor for the curves, and the charge balance, which varies with LLI. Operating boundaries are later defined as the unique conditions which provide the maximum and minimum voltage cut-offs.

After the identification of thermodynamic parameters, a P2D thermo-physical model [15] is applied to identify the value of a selected set of kinetic and mass transport-related parameters, by reproducing tests D1, D2, E1, E2 of the characterisation procedure described in Section 2.3. The following parameters are identified along the campaign (as described below): kinetic rate constant and solid-state lithium diffusion of both electrodes, electrolyte conductivity, film resistance of the negative electrode (simulating the resistance increase due to SEI growth) and double layer capacitance of the positive electrode [19]. Double layer are implemented as an additional current density, in parallel to that of the electrochemical reaction, on the surface of electrode particles, as in Ref. [18]. It depends on the capacitance (property of the layer, constant and uniform) and the overpotential at the electrode-electrolyte interphase. Film resistances are modelled as ohmic 0D resistance on the surface of the particles, inducing an ohmic drop at the interphase electrode-electrolyte. EIS is modelled with the P2D model in the frequency domain to save computational time, though its simulation in the time domain is possible, providing very similar results.

It is also worth reminding that kinetic and diffusion properties depend on the battery temperature and that electrolyte conductivity and diffusivity are linked by means of the Nernst-Einstein relation. Moreover, the P2D model is coupled with a 2D thermal model to include battery self-heating during discharge. The domain reproduces the cross-section of a cylindrical cell. The model includes the heat generation inside te cell and the convection with surrounding ambient air. It draws the temperature distribution inside the cell at each time-step, taking the heat generation rate from the P2D model and providing back the average temperature to the P2D model. This average temperature is then exploited to update the value of diffusive and kinetics properties. For model details, the reader can consult [15].

The PSO-based parameters estimation procedure is a stepwise algorithm, discussed in Refs. [13,15] which consists of the following steps:

1. Thermodynamic aging parameters (*LLI, LAMp, LAMn*) are estimated fitting the full discharge at 25 °C C/10, under the assumption of close-to-equilibrium.
2. Kinetic and mass transport parameters are estimated calibrating the model against the two impedance spectra (E1) and (E2) simultaneously, by optimizing kinetic constants ($k_{p,0}, k_{n,0}$) and the double layer capacitance of the positive electrode, $C_{dl,p}$. HFR value is neglected, in order to only consider the charge transfer resistance.
3. Solid diffusivities ($D_{s,p,0}, D_{s,n,0}$) and electrolyte conductivity (σ_{el}) are estimated calibrating the model against the partial discharges (D1) and (D2). Being SEI layer expected to grow along the aging, its film resistance $R_{film,n}$ is estimated from HFR after subtracting internal electrical circuit contributions and ionic resistance, ensuring consistency beneath electrolyte conductivity and diffusivity, as already mentioned.
4. Step 2 is slightly repeated to adjust kinetic parameters after the estimation of mass transport and resistance parameters performed in step 3, ensuring consistency of the identified solution.

The parameter value is reported as an optimal value and a confidence interval. The first refers to the best fit of the parameter identification process. In contrast, the second refers to a range of values that produce a similar result on the characterisation tests. Role of the confidence interval is thoroughly discussed in Section 3.3 under **Trend of kinetic and mass-transport parameters**, where the results are presented and commented.

2.5. Post-mortem analyses

One cell is opened at the end of the campaign for post-mortem analyses in a glovebox under controlled oxygen and water vapour concentrations. One fresh cell is also opened to visualise the differences. They were discharged at the minimum cut-off voltage with C/10 constant current (CC) discharge and constant voltage (CV) phase down to 1 mA and left to relax at least overnight. Coin cells are fabricated with harvested material after washing in dimethyl carbonate (DMC). Electrodes of 16 mm diameter are punched from different positions of the jelly roll. The separator is a Whatman GF/C 1822–849 of 260 μm thickness. Separator coins are punched and let dry at 80 °C overnight before being inserted in the glovebox. The electrolyte is BASF LP57,

involving a 3:7 EC:EMC mixture with 1mol LiPF6 dissolved. 90 µl electrolyte is inserted, not to limit the performance of the cell. Similarly, lithium chips of large capacity are used.

After at least 12h after coin cell assembly, cycles are performed by means of the Neware BTS4000-5V10mA battery testing system at 21 °C. Nominal coin-cell capacity is computed by scaling the full cell capacity over the active area. Accordingly, the C-rate is computed. The voltage cut-off is chosen arbitrarily depending on the active material. In particular, Graphite: between 0.01V and 1.6V, NMC + LMO (lithium-manganese oxide): between 2.9V and 4.5V. One cycle at nominal C/20 and one at C/50 are performed, but only the latter is investigated in this work.

EIS at 25 °C and different states of charge are performed for at least one sample for each original full cell. They are performed either by means of a Gamry Reference 3000 or Gamry Interface 5000E potentiostats. All cells are positioned in a thermal chamber (Binder MK 53) and left at rest until thermal equilibrium at 25 °C is reached. Then, they undergo a charge (delithiation) phase up to the maximum voltage selected for the quasi-open circuit potential measurements. After 5h of rest, they undergo a sequence of C/10 discharge for 30 min, relaxation for 5h and EIS measurement until the lowest voltage cut-off is achieved. EIS is performed at 5 % or 10 % SoC intervals. Preliminary tests are performed to determine a suitable current amplitude. The frequency range spans from 20 kHz to 10 mHz, with 20 points per decade.

SEM images are taken with different magnifications to identify the size of solid particles and the presence of surficial layers. Moreover, Energy Dispersive X-ray Spectroscopy (EDS) is applied to investigate variations in chemical composition.

3. Results

The experimental and modelling results are described here. Due to the large amount of data, this section is structured in this way:

- First, capacity loss evolution is shown as an overview of the effect of the operating conditions.
- Second, an in-depth analysis of one sample is provided, in particular:
  - o Evolution of the quasi-equilibrium discharge upon cycles with model simulations.
  - o Evolution of high C-rate discharges and EIS with model simulations.
  - o Proposal of physical interpretation of results.
- Lastly, a comparison of physical parameters' trends among different samples is provided to highlight the effect of temperature and state of charge.

3.1. Capacity loss

The capacity loss Q_{loss} evolution of all the cells is displayed in Fig. 2a (panel a: ageing at 60 °C and 25 °C, panel b: ageing at 45 °C), computed as

$$Q_{loss} = \frac{Q_{BOL} - Q_{act}}{Q_{nom}} \quad (1)$$

where Q_{BOL}, Q_{act} and Q_{nom} are the measured capacity at begin of life (BOL), the one at a certain ageing state and the nominal capacity from the datasheet, respectively. Different colours identify different SoCs, whereas different markers and line styles refer to different temperatures. It is possible to state how both high temperatures and high SoCs trigger a faster degradation, as expected [1,3]. To enable a quantitative analysis of the aging trends and to identify the proper time dependence, three fitting approaches were investigated: namely, a linear fit with zero intercept, a square root of time with zero intercept and a linear fit excluding the first point (null capacity loss at the beginning) and considering the y-intercept as a fitting parameter. The charts with measured data and fitting lines for the first two methods are reported for brevity in Figure S1 of the Supplementary Materials associated with this

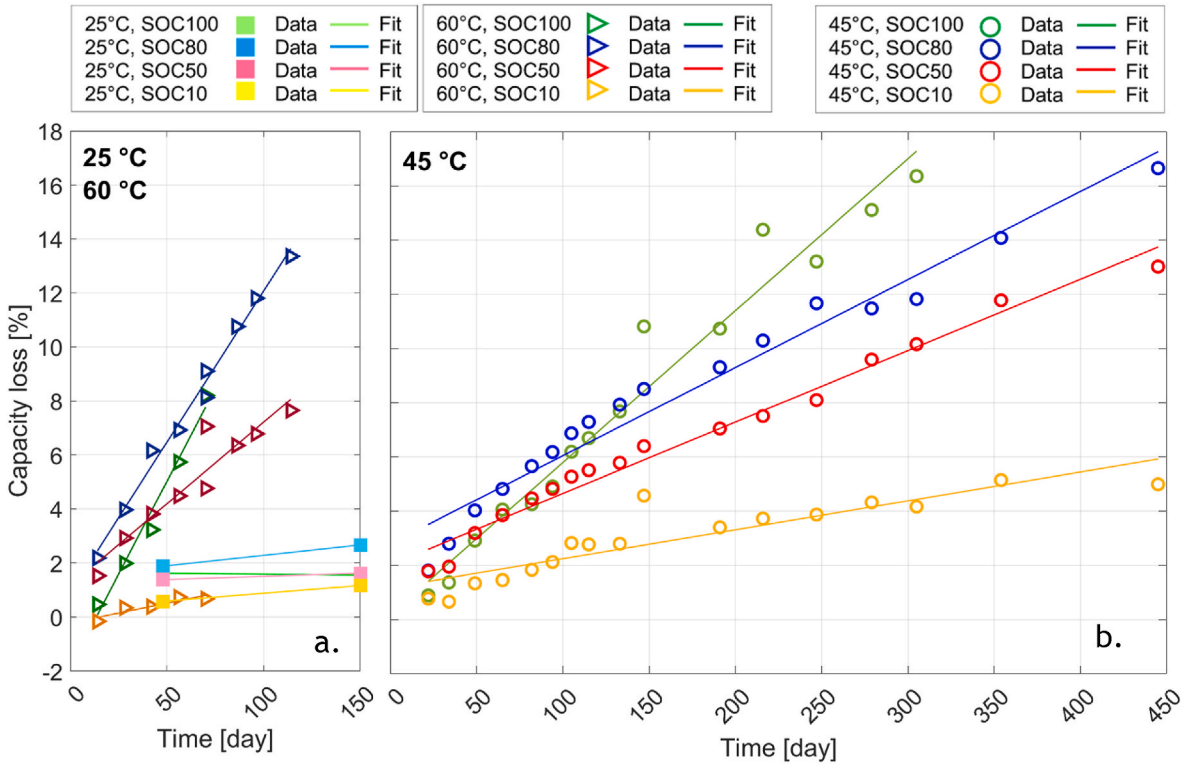

Fig. 2. Capacity loss evolution vs time of all cells. Solid lines for "linear fit neglecting the first point" fitting strategy, markers for experimental data. a) Ageing test at 25 °C (triangles) and 60 °C (squares), b) ageing test at 45 °C (circles).

manuscript, while the third case is directly shown in Fig. 2 (solid lines). The development of a capacity loss model is out of scope for this work. The results of the fitting analysis are reported in Table 3. R^2 is exploited as an indicator of the reliability of the fitting method.

The first two approaches are inspired by literature [3,4,16]. The linear function provides superior performance (i.e. larger R^2) at 60 °C, where the trends look linear (see Figure S1a of the Supplementary Materials), while the square root function works better at 45 °C, where there is a clear flattening after the steep loss at the beginning of the campaign (Figure S1b of the Supplementary Materials). On the contrary, the third way looks universal and outperforms in all the conditions. At 60 °C, the improvement for R^2 is limited with respect to the linear fit since the slope varies little between the two cases. Anyway, the degree of freedom of the intercept provides more flexibility, especially at extreme SoCs where the linear function shows a low R^2. It is also comparable to or better than the square root function at 45 °C, where the initial step is absorbed in the intercept value. The last approach the best fit and is considered in the following section. A possible explanation for the meaning of the intercept will be provided in the next section, exploiting physical models. Regarding the slopes, there is a proportionality between the SoC and the magnitude of the coefficient. Similarly, higher temperatures lead to larger coefficients at a prescribed SoC, as expected. Nevertheless, it is not possible to identify a single scaling factor due to neither SoC nor temperature dependence. In general, it is possible to state that at high SoC, the capacity loss rate at least doubles between 45 °C and 60 °C.

In the next sections, a more in-depth analysis is conducted by exploiting data from check-up procedures and physical models, covering thermodynamic, kinetic and mass-transport phenomena.

3.2. Thermodynamic analysis

Evolution of DV The analysis of the thermodynamic behaviour is presented here through the differential voltage (DV) over a full C/10 discharge. The nomenclature of the main peaks and valleys is reported in Figure S1 of the Supplementary Materials for the fresh state. In the following, the data regarding the sample that was stored at 45 °C and 80 % SoC are presented as an example. Indeed, this sample experienced significant degradation and was included in the validation campaign (Section 4). Moreover, all the cells show similar trends, though at different rates; thus, they are representative of a general calendar-aged cell.

Fig. 3a shows the discharge curve at C/10 and 25 °C at various ageing states in dashed lines, reflecting the capacity loss trend already discussed. For a deeper view, Fig. 3b refers to the corresponding differential voltage curve. Three main trends are identified:

- The low SoC peak (F3) related to graphite shifts to the left.
- Peak F2 shifts to the left, too, almost splitting into two peaks in the last measurements. However, its movement looks slower than that of peak F3.
- The valley at 0.25Ah and the following peak F1 shrinks a bit.

The PSO algorithm is applied to identify the set of thermodynamic parameters that best reproduce the experimental data. The simulations are reported in full lines in Fig. 3a–b, and root-mean squared errors (RMSEs) between experimental and simulated discharge curves are reported in Table 4. The model shows satisfactory agreement with the experiments, aligning the relevant peaks and valleys properly, resulting in RMSE values always within 1 mV and 8 mV. Thus, it is worth investigating the trends of physical parameters that are associated with this result.

Thermodynamic parameters evolution Evolution of the physical parameters over time is showed in Fig. 4a. First, clear trends emerge despite confidence bands (explained in Section 2.4). There is a clear growth of LLI, which is almost linear in time after an initial large growth in the first 35 days. A steep growth of LAMn is estimated in the first 100 days, which then stabilises at ~8 %. Lastly, LAMp also grows linearly.

LAMn is characterised by a similar trend in all the tested cells in all the operating conditions, as already discussed in the low-temperature charging campaign on the same cell type. This trend is verified with a charge-based method in Section S3 of the Supplementary Materials. This fast increase followed by a flattening is interpreted as a stabilisation process of the material, which might have needed some further activation cycles which were not part of the initial characterisation procedure.

On the other hand, LAMp in a calendar ageing campaign can be associated with transition metal dissolution, cathode electrolyte interphase growth (CEI) or cation mixing, promoted by long storage time at high temperature and voltage [20–23]. Lastly, LLI can be linked to at least two terms: the loss of cyclable lithium due to side reactions with the electrolyte, which may form surface layers like SEI, and the lithium loss due to active site loss in the electrodes [1,23–26]. Indeed, as explained in Section 2.4, LAMs are implemented as purely delithiated in the model and lithiated LAM is considered a suitable superposition of LLI and delithiated LAM. In calendar ageing, a reasonable assumption is allowed regarding the lithiation level in the electrodes when LAM occurs, related to the condition of storage.

Fig. 4b reports the bar chart with the share of lithium loss due to lithiated positive and negative LAM (blue and red bars, respectively) and the remaining amount, which can be associated with side reactions with the electrolyte. Lithiation levels in the electrodes are estimated for the fresh cell and kept equal for the aged cell. For simplicity, a storage SoC equal to 5 % lower than the nominal one is considered to take the electrode slippage due to lithium loss into account. Lithiated LAMn is almost constant due to a constant LAMn. The cell stored at 80 % SoC has a significant lithiation level in graphite, inducing a 5 % lithium loss. Its relative share is significant at the beginning, while it decreases along the campaign. The contribution of the positive electrode is linear over time as LAMp, and it becomes the largest part of the last stages. The sum of both terms always exceeds 50 % of the total lithium loss. The portion that is associated with the electrolyte side reactions has a linear trend, but in the first stages, it is negative. This is unphysical and can be associated with a few reasons. The lithiation level in the positive electrode was assumed since positive electrode half-cells are not cycled until the fully delithiated condition. A lower lithiation degree can be reasonable. Second, the estimation of LAMs is uncertain. For instance, LAMn after 34 days of calendar ageing is lower than after 22 days, which is also unphysical. This variability translates into uncertainty regarding the corresponding lithium loss contribution. Lastly, phenomena like

Table 3
Fitting of capacity loss trends for the calendar ageing campaign. "Coeff" for coefficient, "Interc" refers to the intercept with the y-axis. Coefficients in day^{-1} and $day^{-0.5}$for linear and square root fits, respectively.

Cell	Linear fit		Square root fit		Linear (neglect the first point)		
	Coeff	R^2	Coeff	R^2	Coeff	Interc	R^2
45 °C, 100 % SoC	0.061	0.945	0.598	0.750	0.056	0.177	0.963
45 °C, 80 % SoC	0.044	0.839	0.702	0.965	0.033	2.788	0.964
45 °C, 50 % SoC	0.034	0.875	0.550	0.953	0.026	2.010	0.979
45 °C, 10 % SoC	0.015	0.663	0.250	0.896	0.011	1.176	0.808
60 °C, 100 % SoC	0.101	0.922	0.689	0.703	0.137	−1.843	0.978
60 °C, 80 % SoC	0.123	0.985	1.081	0.910	0.112	0.876	0.989
60 °C, 50 % SoC	0.075	0.897	0.668	0.912	0.060	1.167	0.896
60 °C, 10 % SoC	0.010	0.807	0.071	0.633	0.015	−0.218	0.842

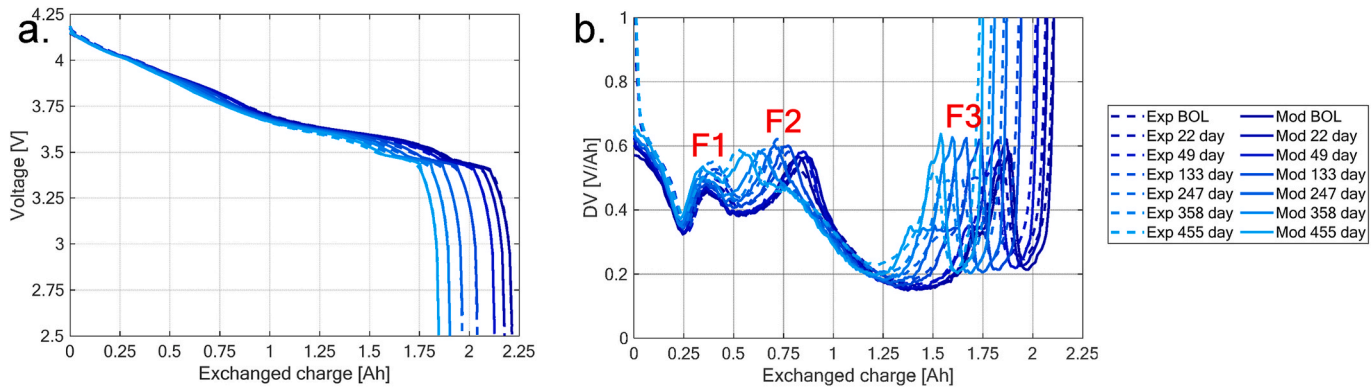

Fig. 3. Experimental (dashed lines) and modelled (full lines). a) Discharge curve and b) differential voltage of the cell stored at 45 °C and 80 % SoC at various check-ups.

Table 4
RMSE values for C/10 discharge curves simulations.

Ageing	RMSE [mV]
Begin-of-life	2.7
22 days	3.1
49 days	7.6
133 days	2.9
247 days	4.1
358 days	5.2
455 days	1.9

anode overhang cannot be excluded from this analysis. Overall, this analysis is not exactly quantitative, but it highlights the significant role of LAMs. Moreover, the lithiated LAMp trend is not as steep as the term associated with electrolyte consumption. Thus, it is possible to predict a larger share of side reactions, e.g. SEI growth, over the total lithium loss if the campaign is further pursued. Lastly, it is possible to associate the initial large capacity loss, observed in Section 3.1, with the contribution of lithiated LAMn.

3.3. Kinetics and mass transport

Experimental trends The operation of the cell in the different characterisation tests is reported at various ageing states in Fig. 5. As described in Section 0, the measurements include two EIS measurements and two partial discharges. Fig. 4a shows a significant increase in the high-frequency intercept with the x-axis (or high-frequency resistance, HFR). In the last stages, a variation of around 30 % is detected. Moreover, an increase in the kinetic loop is also present. Fig. 5b shows that at least one reaction is shifting towards a lower frequency, thus widening the magnitude of the semicircle. No difference is present for frequencies larger than 100Hz and lower than 1Hz.

These trends become more significant in Fig. 5c–d (i.e. at lower temperatures and higher SoC). The evolution of the spectrum is much stronger. The minimum after the kinetic loop is not present anymore, and the value of the impedance steadily increases with the calendar's time. The separation between kinetic and diffusive regions becomes indistinguishable. Moreover, the frequency of the phenomenon is lower and affects the diffusive area, too.

Fig. 5e–f shows the behaviour during discharge. In Fig. 5f, the capacity reduction and an increase of the overpotentials are detected. Furthermore, Fig. 5e shows a particular profile. In the first seconds, a linear decrease of voltage is observed until it forms a plateau. A model is required to understand the physics behind this phenomenon. However, the plateau may be associated with a large temperature increase inside the cell, which counterbalances the large overpotentials of the first part. The losses are so large that the voltage approaches the minimum voltage cut-off at SoC 50 %.

Modelling results The parameter identification procedure explained in Section 2.4 is applied here to identify the set of parameters reproducing the experimental trends. The simulations of the tests belonging to the characterisation procedure are reported in full lines in Fig. 5. To quantify the reliability of the simulations, RMSE values are reported in Table 5. The simulations of both impedance spectra (Fig. 5a–b for EIS measurement E1, Fig. 5c–d for E2) are consistent. The shift of the HFR, the growth of the loop and the decrease of its characteristic frequency are well reproduced. In the last stages, the model underestimates the further shift towards low frequency, but there is a general and strong agreement both in frequency and magnitude. In the 2C 10 °C discharge (Fig. 5e, discharge D1), the model follows the main trends, with the increasing losses and the flattening of the curve. However, in the last stage of degradation, the losses are underestimated. This is a consequence of the multiple constraints of the parameter identification procedure. Indeed, the 1C 25 °C (Fig. 5f, discharge D2) is reproduced in a satisfactory way. Additional losses in Fig. 5e would translate into excessive losses in this case. The model simulates both the reduction of the extractable capacity and the increase in losses. Results are considered satisfactorily under both a qualitative and quantitative point of view.

Trend of kinetic and mass-transport parameters The simulations of the characterisation tests are satisfactory. Therefore, the corresponding evolution of physical parameters is exploited to derive the interpretation. Trends of physical parameters are reported in Fig. 6. Electrolyte conductivity (Fig. 6a) decreases almost linearly over time. Its trend is responsible for a relevant portion of losses in the discharge, as well as an increase of the HFR value and of the impedance around 10Hz. Its trend is quite defined (little confidence band). This trend is consistent with a decomposition of the electrolyte, driven by high voltage and temperature, forming either gasses or SEI [1,4]. In this regard, it is worth noting that the negative film resistance (Fig. 6g) also linearly increases over time, but this trend is not so clear for all the cells that underwent calendar ageing.

Positive electrode kinetic parameters are slightly affected by storage. The kinetic rate constant (Fig. 6e) decreases linearly, while the capacitance of the double layer (Fig. 6b) shows a noisy trend, slightly growing on average. These parameters mimic the evolution of EIS. Indeed, the kinetics of the negative electrode is quite constant (Fig. 6f). Its value lies always in the confidence band of the fresh cell. Moreover, due to the separation of the kinetic loop into two separate entities, its value becomes more defined (lower width of the confidence band) along the campaign. The algorithm associates the mid-high frequency loop to the negative electrode charge transfer and the mid-low to the positive electrode. This situation comes from the assumption of constant double-layer capacitance on the surface of graphite, which is discussed in Section S3 of the Supplementary Materials, taking into account the

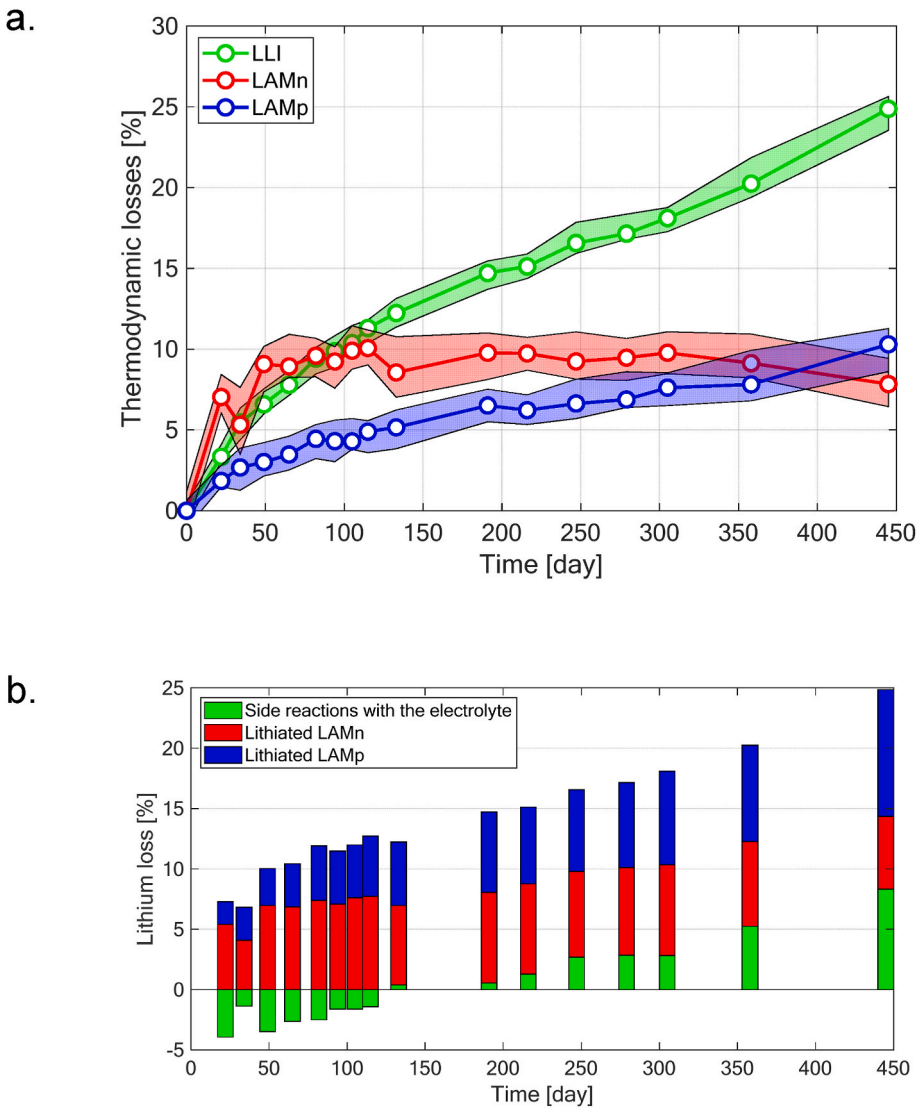

Fig. 4. a) Trend of the thermodynamic parameters and b) shares of lithium loss of the cell stored at 45 °C and 80 % SoC.

impedance of half cells of fresh and aged materials. Here, it is clear that the impedance of the negative electrode is almost unchanged despite calendar ageing, while the positive electrode impedance has some differences. This assumption induces the constant trend of the kinetic constant since the mid-high frequency part of the experimental EIS is constant.

Lastly, lithium solid-state diffusivity into the positive electrode (Fig. 6c) has a decreasing trend. The algorithm identifies this parameter as responsible for the flattening of the voltage of the 2C discharge at 10 °C. Its evolution is stronger at the beginning and then stabilises.

On the contrary, the property of the negative electrode has a growing trend (Fig. 6d), by more than one order of magnitude. This trend is not discussed in the literature to the best of the authors' knowledge. One possibility refers to a lower dimension of the particles. For instance, particle cracking occurs, improving lithium diffusion in the solid state, thus reducing the mass transport limitations and the corresponding overpotentials, which are important in the final stage of the discharge, where graphite is almost delithiated. This trend was already discussed in Ref. [14], linking its trend with the evolution of LAMn and of the residual capacity at 1C. The reader is referred to this work for additional information.

Before the physical interpretation of the parameters trend, it is worth discussing the confidence bands, which result quite large in some conditions. It is meaningful to trace this range to assess the relevance of a parameter variation due to ageing. If there is a clear evolution of the range, it means that degradation and this parameter are linked.

However, the capability of the P2D model to reproduce experimental curves are challenged at more and more aged states, and so the identification of physical parameters, resulting in a broad band. Moreover, it is worth underlying how the input data are relatively little to save on testing time, but negatively affecting the parameter identification process which would benefit from additional data.

Anyway, large bands appear when the parameter has a relatively high value and this does not affect the reliability of the analysis significantly. This is the case of solid diffusivities. Indeed, in the P2D model the effect of solid diffusivities becomes relevant when they assume relatively low values, meaning that, taking into account the characteristic radius of the solid particles, their value is low enough to induce concentration gradients in the electrode particles, which turn into potential gradients. When solid diffusivity value is relatively high, solid-state diffusion is not slow enough to affect the discharge curve at a significant extent. In this condition, the exact determination of solid diffusivities become more challenging, since their effect is poorly detectable. This is the reason why its confidence band becomes so wide at increasingly aged states: even a variation by one order of magnitude or more is not affecting the solution.

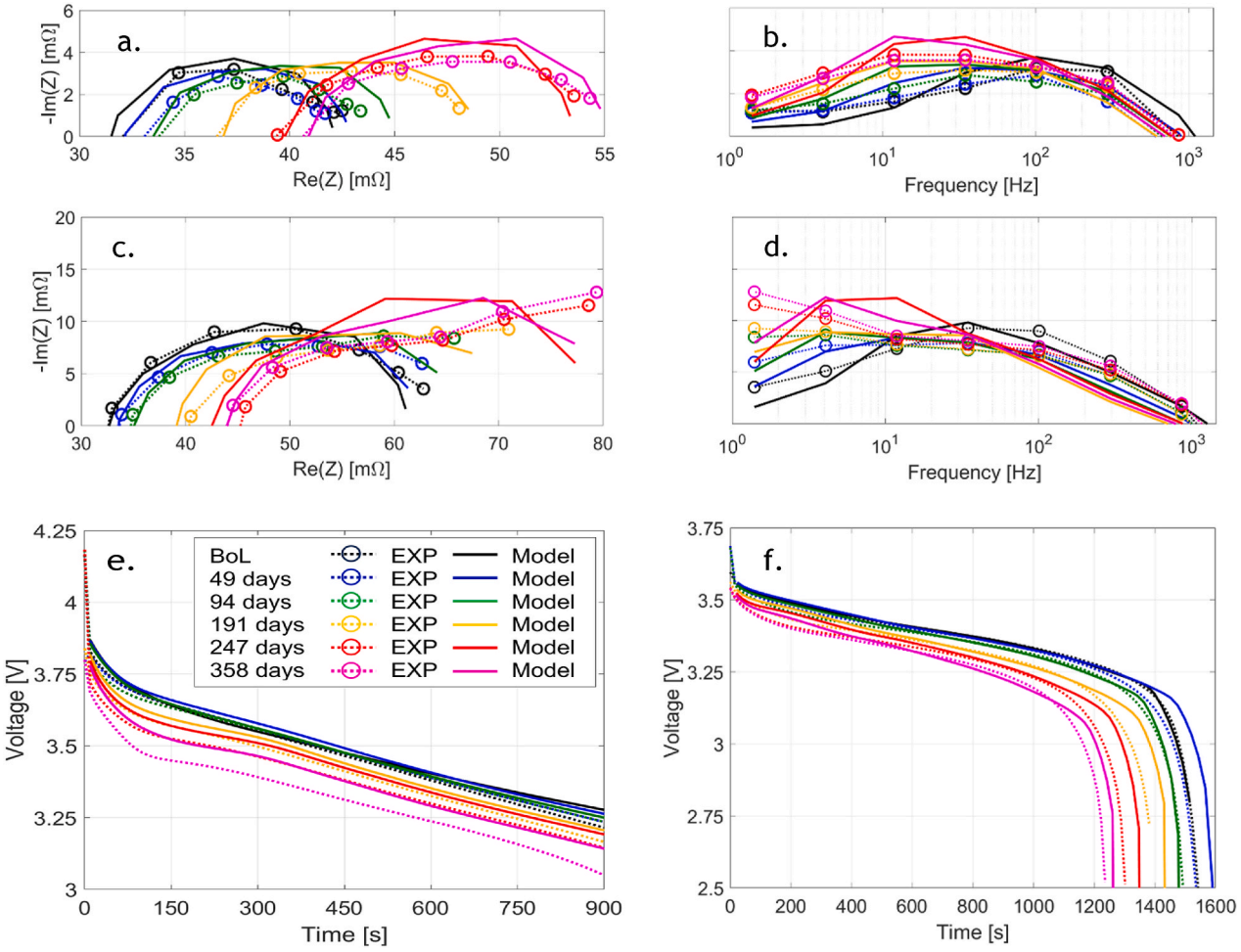

Fig. 5. Experimental (dashed lines) and corresponding simulations (full lines) measurements belonging to the check-up procedure for the cell stored at 45 °C and 80 % SoC: (a–b) Nyquist and Bode plot of the imaginary component of the impedance E1, recorded at 50 % SoC and 25 °C; (c–d) Nyquist and Bode plot of the imaginary component of the impedance E2, recorded at 100 % SoC and 10 °C; (e) discharge D1 at 10 °C 2C, from 100 % to 50 % SoC; (f) discharge D2 at 25 °C 1C, from 50 % SoC to the minimum voltage level. Legend in subfigure (e).

Table 5
RMSE values for EIS and high C-rate discharge simulations, belonging to the characterisation procedure.

Ageing state	E1 [mΩ]		E2 [mΩ]		D1 [mV]	D2 [mV]
	Real	Imag	Real	Imag		
BOL	0.5	1.3	1.5	1.6	29.4	5.9
49 days	0.7	1.3	1.7	1.3	17.5	62.6
94 days	0.9	1.1	2.0	1.6	33.8	15.1
191 days	0.6	0.7	4.2	1.7	26.6	42.9
247 days	0.7	0.9	4.8	2.7	55.4	53.6
358 days	0.8	1.0	3.9	2.4	63.5	40.9

Lastly, the representation with tolerance bands do not show the distribution of the solutions. It is enough that only one solution (out of tens in the 5 % tolerance window) shows one extreme value so that the tolerance band must include that value, even though it looks like an outlier. The tool works in this way for the sake of simplicity and universality.

3.4. Physical interpretation of the modelling results

The analysis of the experimental trends with the support of the model identifies unexpected trends for the parameters of the negative electrode, namely a steep increase of LAMn followed by a plateau and a strong increase of its solid-state diffusivity. These trends, shared by all the cells disregarding the operating conditions, are associated with a stabilisation of the electrode-like particle cracking, which involves the loss of part of the active material on one side and the reduction of the characteristic length for lithium diffusion on the other.

DV analysis highlighted a significant LLI. Its chart shows an initial step, followed by a linear increase in storage time. The first drop might be associated with a lithiated LAMn, while the following evolution is a combination of lithiated LAMp and lithium loss due to side reactions with the electrolyte. A relevant fraction can be associated with the loss of the positive electrode, which is also linear in time. The remaining part of lithium loss is assumed to have undergone side reactions, increasing the thickness of the SEI [1,23–26].

Applying the parameter identification procedure on high C-rate discharge and EIS allows a linear decrease of the electrolyte and a simultaneous increase of the film resistance. Both trends can be correlated with the LLI and the electrolyte's decomposition forming SEI [3,4,23].

The formation of a second kinetic loop in the EIS spectrum is reproduced with a worsening of the kinetics of the positive electrode reaction. At the same time, an important decrease in the solid-state diffusivity of the same electrode is estimated. The combined evolution of these parameters is not commonly discussed in the literature. Stiasny et al. [5] identified diffusional limitations in aged positive electrodes without providing a solid interpretation. Worsening of the kinetics of the

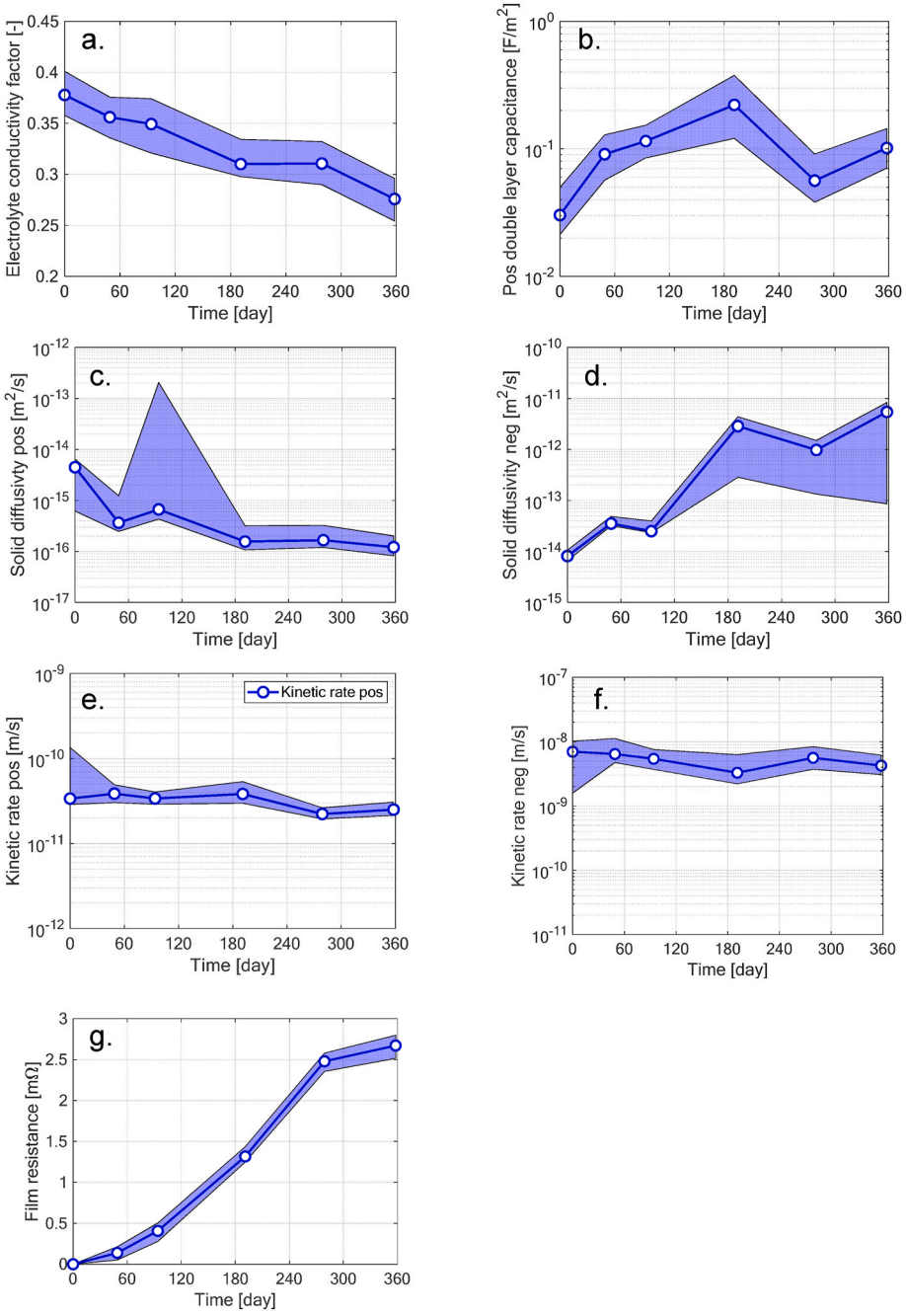

Fig. 6. Trend of the physical parameters over time with uncertainty bands: a) electrolyte conductivity factor, b) positive electrode double layer capacitance, kinetic rate constant of c) positive and d) negative electrodes, solid-state diffusivity of e) positive and f) negative electrodes, g) negative electrode film resistance.

electrode was also observed in previous works, providing different classes of phenomena without a clear validation [20,23]. Possible degradation mechanisms are transition metal dissolution and CEI growth.

3.5. *Effect of storage temperature and SoC*

The role of storage conditions, e.g. temperature and SoC, are now investigated by comparing these results (storage at 45 °C and 85 % SoC) with that of the other two cells, namely:

- The cell that was stored at 60 °C and 80 % SoC, to highlight the role of temperature.
- The cell that was stored at 45 °C and 50 % SoC, to highlight the role of SoC.

We avoided 10 % SoC since the degradation rate is much lower and the cells seem close to a fresh state. On the contrary, all cells stored at 100 % at both temperatures experienced a significant self-discharge, which inhibits their extensive investigation.

Effect of storage temperature The most important trends are reported in Fig. 7. LLI is larger for higher temperatures, consistently with SEI growth and the formation of gases, which are promoted by high temperatures [1,23]. Its trend is similar to the capacity loss. The increase of LAMp (Fig. 7a) is favoured by high temperature, too. The voltage threshold of stability of layered oxides decreases as ambient temperature increases. Thus, this trend is consistent [23]. Furthermore, electrolyte conductivity (Fig. 7b) is observed to decrease faster at high temperatures. This trend is again consistent with a faster consumption of electrolytes [1,23]. The last two trends are less straightforward. The rate

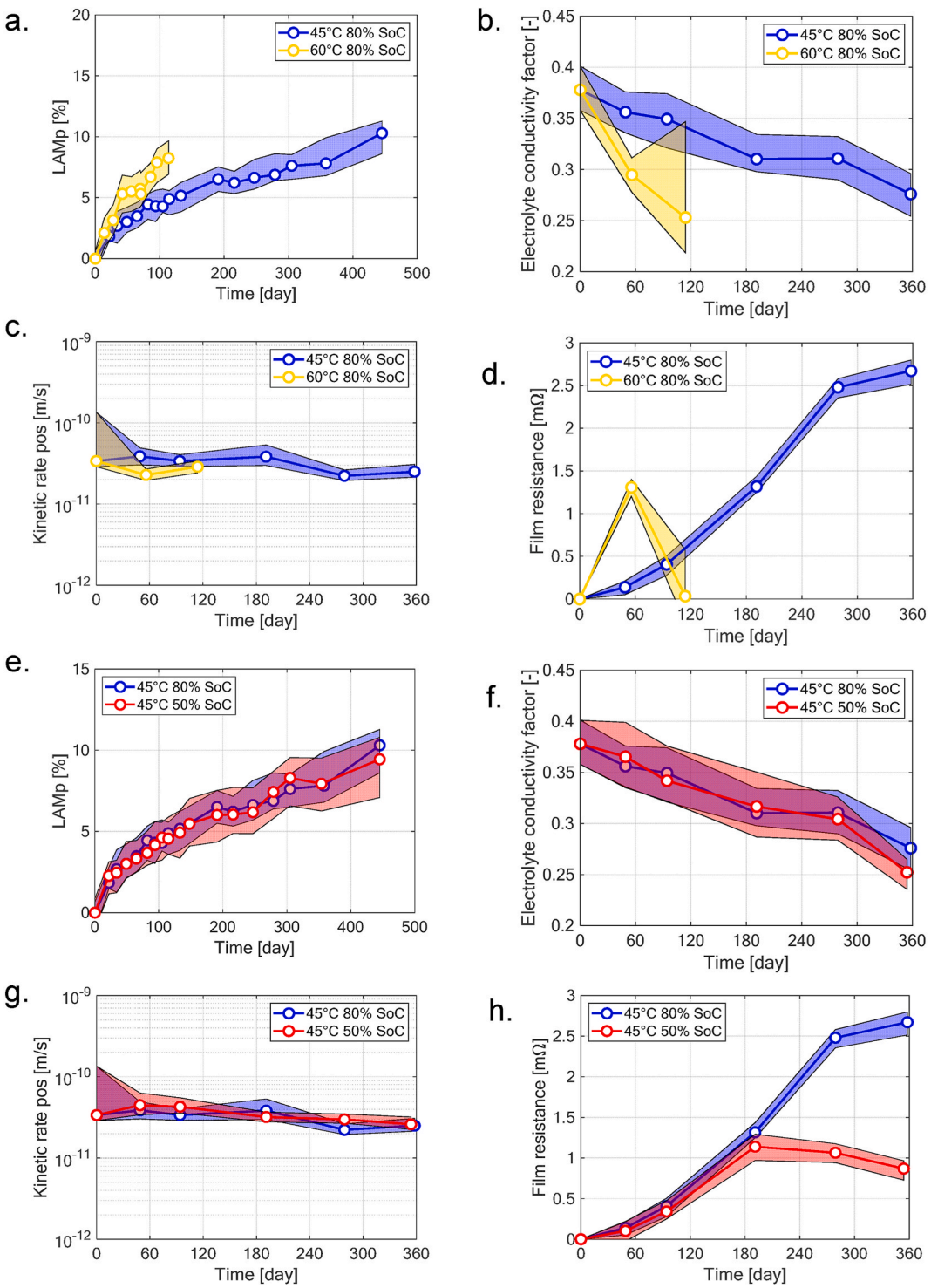

Fig. 7. Effect of temperature (a–d) and SoC (e–h) on storage. Trend of some physical parameters over time for storage 80 % SoC at 45 °C (blue curves), 80 % SoC at 60 °C (yellow) and 50 % SoC and 45 °C (red), with uncertainty bands: a) and e) loss of active positive electrode material; b) and f) electrolyte conductivity factor; c) and g) kinetic rate constant of the positive electrode; d) and h) film resistance of the negative electrode. (For interpretation of the references to colour in this figure legend, the reader is referred to the Web version of this article.)

of decrease of the kinetic constant of the positive electrode is slightly larger at 60 °C than at 45 °C (Fig. 7c). This is consistent with the evolution of EIS, which appears to be poorly affected by storage in general. Lastly, film resistance shows some noise (Fig. 7d). It appears to be larger than the corresponding value for 45 °C storage, but its trend is not clearly defined.

All these trends are confirmed if the comparison is performed between storage at 50 % SoC at 45 °C and 60 °C. In particular, the kinetic rate constants are separated and the evolution of film resistance is monotonic, with a larger drop at 60 °C. Overall, temperature affects the growth of the SEI, with multiple effects on the lithium inventory, the electrolyte conductivity and the film resistance. Moreover, the degradation of the positive electrode is accelerated, too.

Effect of storage SoC The most interesting parameter evolution

related to the effect of the SoC is depicted in Fig. 7e–h. It is worth understanding how LAMp does not vary if the storage SoC is changed between 80 % and 50 % (Fig. 7e). This result is unexpected, but the same conclusion is derived if the same comparison is performed between 80 % and 50 % at 60 °C (not shown for brevity). Similarly, electrolyte conductivity follows the same linear trend despite graphite being expected to operate on two different stages: the first plateau for the cell at 80 % SoC and the second for 50 % SoC. Again, the same result is derived for the couple at 60 °C. The effect of SoC is also negligible on the kinetics of the positive electrode reaction, whose kinetic constant is reported as an example in Fig. 7g. The only difference occurs in film resistance (Fig. 7h). However, the cells share the same trend at the beginning, while they differ at the end, where the electrolyte conductivity slightly changes. As already stated in Section 3.3, the model underestimated the losses in the last stages of the cell at 80 % SoC. As a result, this difference in film resistance is likely to be negligible since the experimental impedance is quite similar between the two samples. At 60 °C, this trend is noisy, but the values are quite close.

In conclusion, there is no significant difference between storage at 50 % or 80 %, neither at 45 °C nor at 60 °C, other than additional lithium loss. However, it is noteworthy that 100 % of SoC leads to self-discharge, while 10 % shows very little degradation. It is, therefore, possible to state that there is a beneficial effect in exploiting a low SoC of storage, although this effect is not linear with SoC.

4. Validation of the results

One fresh cell and one aged cell (aged at 45 °C, 80 % SoC) were opened in the inert environment as described in Section 2.5 to perform ex-situ analyses that can verify the interpretation of degradation. Pictures of portions of the jelly roll are reported in Figure S.5 of the Supplementary Materials. In particular, the separator looks yellowish, suggesting degradation of the electrolyte. Harvested materials are then exploited to perform post-mortem analyses.

4.1. Validation of thermodynamic parameters with half-cells

Half-cell Quasi-OCP Half-cells of harvested materials are cycled to validate the value of thermodynamic parameters. First, the investigation of half-cell cycles is performed. Fig. 8 shows the DV plots of both lithiation and delithiation phases of positive (leften sub-figures) and negative (righten) electrodes for harvested material from the fresh and aged samples. Some half-cells are reported for all the cases. Shades identify different positions along the roll: light colour for coin cells that were punched close to the mandrel, dark colour for the outer edge. Intermediate intensity is needed for intermediate positions along the role. DV is chosen because it magnifies the voltage trend while showing capacity variations. From left to right, voltage decreases (i.e., lithium concentration in the material increases): lithiation and delithiation processes are reported in red and blue, respectively.

First, the two phases have different capacity values, possibly related to a slight self-discharge. This difference is in the order of 3–4%. The cell-to-cell variability in the same phase has a maximum of 5 % and 5.5 % of capacity retention in discharge and charge, respectively. If plotted against a normalised charge value, all curves overlap, showing a good reproducibility of the measurement. The shape of the curves highlights the phase transitions of LMO and NMC materials, as reported in Figure S.1 of the Supplementary Materials.

The same data are presented for five coin-cells of graphite. The cell-to-cell variability of capacity is 7 % at maximum for both phases, but all the curves almost overlap if they are represented against the normalised charge. No significant difference between the discharge and charge phase is evident, consistent with a self-discharge mechanism, since NMC + LMO cells work at significantly higher voltage levels with respect to graphite ones. The curves show a hysteresis (e.g. the shape of the peak around 3.5mAh and around 6.5mAh). The staging behaviour of graphite is easily identified.

For the aged positive electrode, the shape is preserved, but the amount of exchanged charge is variable. The cell-to-cell variability of exchanged capacity is estimated to be within 7 %, exploiting eight coin cells each. Regarding negative electrodes, the shape is preserved, together with the hysteresis between lithiation and delithiation phases. The variability of exchanged charge between half-cells of the same original cell is estimated within 14.4 % over 11 half-cells each. There is a slight general tendency to provide lower performance for cells that were punched close to the mandrel. Overall, the value of capacity is

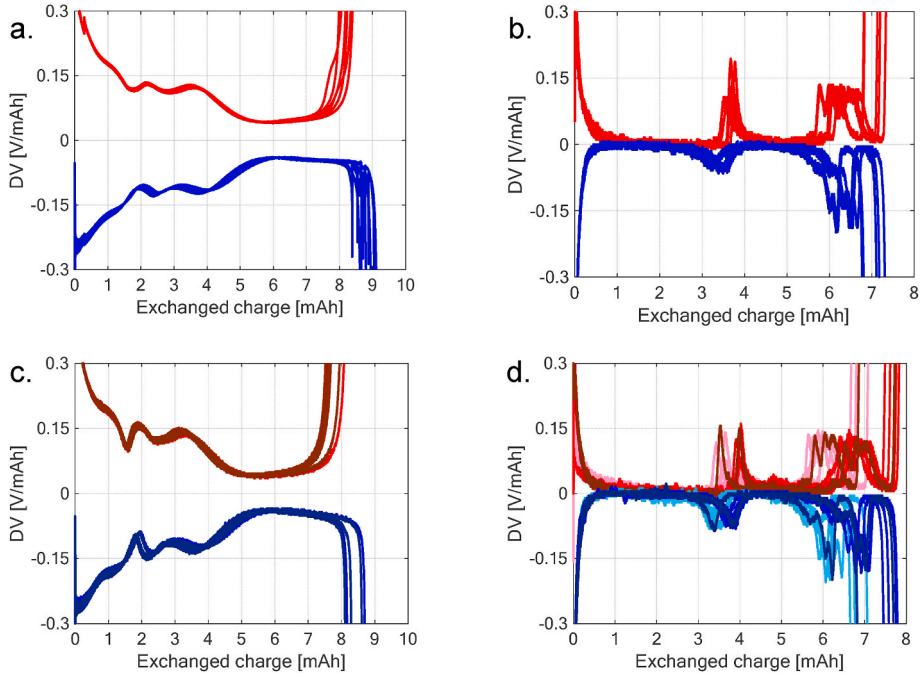

Fig. 8. C/50 lithiation (red curves) and delithiation (blue) DV curves of positive (leften subfigures) and negative electrodes (righten subfigures) of the fresh cell (a–b) and aged cell (c–d), respectively. (For interpretation of the references to colour in this figure legend, the reader is referred to the Web version of this article.)

comparable with that of the fresh cell, indicating a narrow level of degradation of the electrodes.

These charts can be represented in relative terms, scaling the DV to the extractable capacity of the half cell. Such manipulation enables the verification of the stability of the OCP curve towards ageing, which is a paramount assumption of the equilibrium model: OCP curves can be stretched and shifted with respect to the other electrode, but the shape (i.e. the relation between the lithium content in the material and the corresponding electric potential) does not change due to degradation. Moreover, it is of particular interest for the positive electrode: if the OCP curve has little variation, the degradation that LMO and NMC experience is similar. Thus, it enables the model of the blended electrode to be a single equivalent material. The normalised plot for one half-cell of positive and negative electrode is reported in Figure S.6 of the Supplementary Materials.

Estimation of half-cell LAM LAM can be estimated from the capacity retention of half-cells. As a matter of fact, coin cells of harvested aged material have the same geometrical dimensions as a coin cell with fresh material. Considering the large excess of lithium corresponding to the lithium counter electrode, a variation of capacity can be related to a decreased acceptability of lithium in the host structure. However, the variability between coin cells is taken into account to avoid mistaking, including this effect in the estimation of LAM. To overcome this problem, the specific capacity is computed. The weight of the single-coated current collector (i.e. one layer of electrode over the total thickness of the current collector foil) is measured experimentally before coin cell assembly. The current collector alone is measured, too, at the uncoated parts at the edges of the roll. The following formula is later applied to estimate the electrode-only mass m_{el}.

$$m_{el} = m_{el+cuc} - A_{coin} \bullet L_{cuc} \bullet \rho_{cuc} \tag{2}$$

where m_{el+cuc} is the measured weight of electrode coating and current collector together, A_{coin} the area of the coin cell, L_{cuc} the thickness of the uncoated current collector and ρ_{cuc} the density of current collectors material (copper and aluminium, respectively, at negative and positive electrodes). The half-cell capacities are plotted against the electrode mass in Figure S.7 of the Supplementary Materials. The scattered data can be ordered with a linear fit (dashed lines), passing through the origin of the axes. The slope of the fitting line is the specific capacity. Finally, the LAM of the electrode i (positive or negative) of the cell j is estimated by comparing the slopes of the fitting line with that of the fresh cell as

$$LAM_{i,j} = 1 - \frac{Q_{ms,i,j}}{Q_{ms,i,fresh}} \tag{3}$$

where $Q_{ms,i,j}$ is the specific capacity of the aged electrode and $Q_{ms,i,fresh}$ the corresponding value for the fresh cell.

The results are provided in Table 6. For the results of the algorithm, the extreme values of the confidence bands are also reported. Interestingly, the estimation of LAMp lies within the interval that is identified by the algorithm. On the contrary, LAMn has a variability, where the algorithm overestimates the loss. However, considering the experimental datum's accuracy and possible variations due to the cleaning procedure before coin cell assembly (Section 2.5), the results are considered satisfactory.

Table 6
Comparison between the estimation of LAM from half-cell cycling (Exp) and the results of the parameter identification procedure with PSO in terms of optimal value and range.

Property	Exp	Min	Optimal	Max
LAMp	7.0 %	6.8 %	7.8 %	9.9 %
LAMn	6.6 %	8.2 %	9.1 %	10.9 %

4.2. Validation of the interpretation through imaging and EDS

Negative electrode Lastly, SEM images and compositional analyses are performed using the techniques described in Section 2.5. Two SEM magnifications (1000x and 5000x) are reported for both fresh and aged samples for comparison in Fig. 9. In Fig. 9a–b, the electrode structure looks quite rich in solid bulky particles in the order of 10 μm of radius. This is consistent with the high-energy design, which aims at maximising the solid material part. Fig. 9c does not show major effects on particle size and shape for the aged cell, but an interesting semi-transparent layer covering all the particles and some white spots. These features are further magnified in Fig. 9d. EDS analysis is carried out in parallel (Table 7). The fresh sample shows a large presence of carbon, with a 5 % fraction of oxygen, as expected. Differently, the aged sample is associated with a lower relative share of graphite, which is replaced by a significantly larger oxygen content (19.5 % vs 5.6 % of the fresh cell in Table 7) and a slightly higher fluorine share. Comparing this result with the literature [8,27], these features can be reliably associated with the growth of SEI, which grows widely and uniformly thanks to the simple storage ageing that is undergone [9,23]. This finding supports the trends of LLI and electrolyte conductivity factor and their interpretation.

The white spots are investigated with a dedicated chemical analysis that is restricted to the surrounding area. The results are reported as "Aged negative (white spot)" in Table 7. With respect to the average analysis, there is a great drop in carbon content and a growth of oxygen, together with the transition metal of the positive electrode, namely Ni, Co, Mn, in a similar atomic ratio as observed in the positive electrode composition (discussed in the following paragraphs). It is very clear that this spot is an agglomerate of NMC powder. It would appear that some crossover of positive electrode material has occurred. However, this characteristic is not considered reliable since it is not possible to ensure that no contamination between samples has occurred during the positioning of the instrument.

Positive electrode Two SEM magnifications are reported for each sample. Fig. 9e–f highlights the presence of two types of microstructures: one bulky particle in the order of 8 μm by diameter and one of ~1 μm. However, a deeper view (Figure S.8b) in the Supplementary Materials indicates that the first class is composed of a dense cluster of particles of the second type. We can conclude that there are large secondary particles and small primary particles of the same type. Moreover, chemical analysis underlines that there is no difference in composition between bigger and smaller particles since the manganese content (Figure S.8c of the Supplementary Materials) does not show inhomogeneities between the big particles and the surrounding smaller ones. This finding is of particular interest since it suggests that modelling the blended electrode with only one characteristic dimension can be a viable approach.

Neither in the large view (Fig. 9g) nor in the zoomed one (Fig. 9h) the material of the aged cell shows major differences with respect to the fresh electrode. Neither surface modifications nor surface layers are visible. The chemical composition is outlined in Table 7. The chemistry seems to be a blend of NMC 532 together with LMO. The carbon share can be associated with conductive additives like acetylene black. The chemical analysis of the aged sample confirms that similar elements were shared with respect to the fresh material. We can conclude that chemical degradation is negligible.

4.3. Final remarks of the validation activity

The interpretation of degradation is verified through some techniques to validate the suitability of the diagnostic methodology in identifying the degradation phenomena according to the evolution of physical parameters. First, the cycling of half-cells with harvested material enabled the verification of the LAM value at the end of the campaign by estimating the specific capacity of the aged material and scaling it to the value of the fresh cell. Considering the uncertainty, the experimental value is close enough to the model value, supporting the

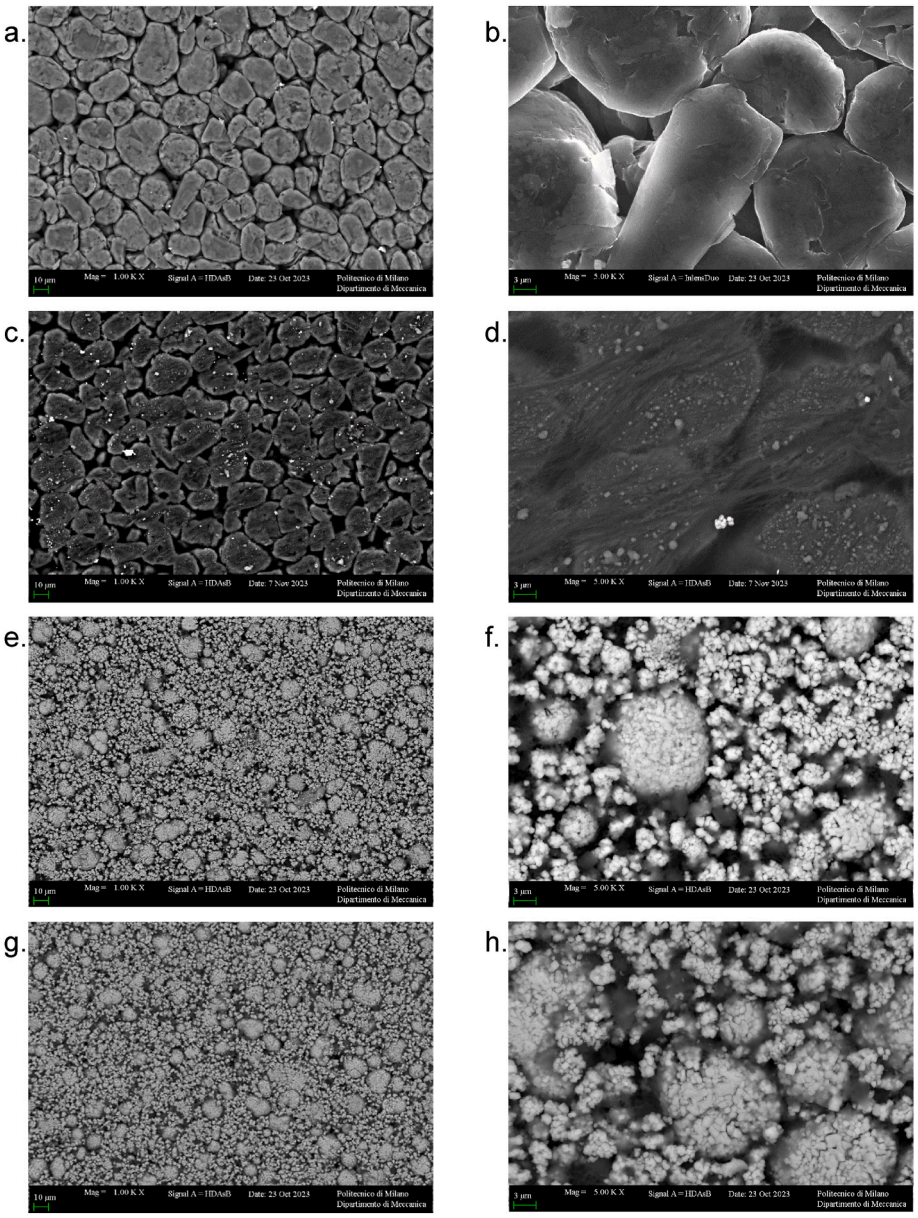

Fig. 9. SEM images of fresh and aged electrodes at 1000x (leften subfigures) and 5000x (righten) magnifications. Lens type in the legend under the subfigures. Negative fresh (subfigures a-b), negative aged (c–d), positive fresh (e–f) and positive aged (g–h).

Table 7
Chemical composition by atomic mass. If not specified, quantities are averages over ~1 mm^2 areas. Elements associated with very low shares are neglected to improve readability.

Original cells	Element atomic fraction [%]								
	C	O	F	Al	P	Mn	Co	Ni	Cu
Fresh negative	91.12	5.65	2.67	0	0.35	0	0	0	0.16
Aged negative	75.99	19.51	3.38	0.03	0.71	0.06	0	0.03	0.17
Aged negative (white spot)	28.76	49.82	0	0.25	0.1	6.11	3.99	10.3	0.68
Fresh positive	42.04	31.43	14.27	0.12	0.33	4.45	2.1	5.26	0
Aged positive	41	28.5	16.4	0.1	0.5	5.02	2.41	6	0

thermodynamic analysis. The flattening of LAMn is further investigated by means of a charge-based method on the differential voltage curve, and the results show a good agreement. Lastly, morphological and chemical analyses are reported. Aged cells show a surficial layer and excess oxygen, which can be related to a thick SEI. Moreover, the separator is yellowish, suggesting a significant decomposition of the electrolyte. This evidence supports the occurrence of SEI growth and the trends of LLI, electrolyte conductivity and film resistance. No deterioration of the positive electrode is detected at a significant extent, rather than a moderate LAM and a variation of its impedance.

5. Conclusions

In our experimental campaign exploring calendar ageing, we investigated the impact of temperature and state of charge on the battery performance during operation. This investigation, focusing on a key reference case, has underscored the significant role of high temperature and state of charge in accelerating lithium inventory loss. Additionally, we observed substantial electrolyte consumption across various conditions, directly correlating with low battery efficiency under high C-rate operations. This phenomenon is predominantly attributed to gas release or SEI growth, further complicating battery longevity.

Our analysis reveals that SEI formation is notably exacerbated at high temperatures, leading to a faster lithium loss, a rapid decline in conductivity, and an increase in film resistance. Similarly, degradation of the positive electrode is significantly accelerated under these conditions, primarily due to loss of active material, diffusion limitations, and slightly compromised kinetics, all of which contribute to overall battery inefficiency. Despite minor variations observed between 50 % and 80 % SoC during storage, our subsequent verification through additional measurements and post-mortem analyses solidified our initial findings:

- The determination of thermodynamic parameters was consistent with predictions made from half-cell cycling, affirming the reliability of our methodological approach.
- SEM and EDS analyses confirmed the formation of a uniform and thick SEI layer, corroborating with observed reductions in lithium inventory loss and electrolyte conductivity, further validating our findings.
- Impedance spectroscopy variations were attributed to the positive electrode. Considering that minimal changes are detected in the chemical composition of the positive electrode, it suggests that chemical mechanisms like transition metal dissolution or cation mixing occurred to a limited extent. CEI growth could explain these effects.

Our research conclusively demonstrates the robustness and reliability of our methodology in analysing and interpreting battery degradation mechanisms. The application of physical models proved to be a suitable tool for diagnostic purposes, being able to simulate the most important degradation effects on performance and relate them to the most likely degradation phenomena. The consistency of the results has been verified against post-mortem analyses with successful results.

This study not only provides insightful revelations into the complex interplay between operational conditions and battery longevity but also establishes a solid foundation for future explorations aimed at enhancing battery performance and lifespan.

CRediT authorship contribution statement

Gabriele Sordi: Writing – review & editing, Writing – original draft, Visualization, Validation, Methodology, Investigation, Formal analysis, Data curation, Conceptualization. **Daniel Luder:** Writing – review & editing, Investigation. **Weihan Li:** Writing – review & editing, Supervision. **Dirk Uwe Sauer:** Supervision. **Andrea Casalegno:** Writing – review & editing, Supervision, Project administration, Funding acquisition. **Claudio Rabissi:** Writing – review & editing, Supervision, Project administration, Funding acquisition, Conceptualization.

Declaration of competing interest

The authors declare that they have no known competing financial interests or personal relationships that could have appeared to influence the work reported in this paper.

Data availability

Data will be made available on request.

Acknowledgements

This work was supported by the European Union's Horizon 2020 Research and Innovation Program [Grant Agreement No. 873111, project "DigiPrime - Digital Platform for Circular Economy in Cross-sectorial Sustainable Value Networks"] and the Energy for Motion initiative of Politecnico di Milano as part of Energy department recognition as Department of Excellence 2018–2020 from Italian Ministry of Education, Universities and Research (MIUR).

The authors would like to acknowledge Melissa Sedzik, Andrea Rondi, Davide Conti, Andrea Stecchini and Roberto Evangelista for supporting the experimental campaigns and early simulations. Moreover, the authors would like to acknowledge Ludovica Rovatti and Rasheed Michael Ishola for their help in performing SEM analysis. Lastly, G.S. would like to acknowledge the IDEA League for funding his research exchange at CARL, RWTH Aachen University, Germany.

Appendix A. Supplementary data

Supplementary data to this article can be found online at https://doi.org/10.1016/j.jpowsour.2024.235076.

References

[1] P. Keil, S.F. Schuster, J. Wilhelm, J. Travi, A. Hauser, R.C. Karl, A. Jossen, Calendar aging of lithium-ion batteries, J. Electrochem. Soc. 163 (2016) A1872–A1880, https://doi.org/10.1149/2.0411609jes.

[2] M. Ecker, N. Nieto, S. Käbitz, J. Schmalstieg, H. Blanke, A. Warnecke, D.U. Sauer, Calendar and cycle life study of Li(NiMnCo)O2-based 18650 lithium-ion batteries, J. Power Sources 248 (2014) 839–851, https://doi.org/10.1016/j.jpowsour.2013.09.143.

[3] J. Schmalstieg, S. Käbitz, M. Ecker, D.U. Sauer, A holistic aging model for Li (NiMnCo)O2 based 18650 lithium-ion batteries, J. Power Sources 257 (2014) 325–334, https://doi.org/10.1016/j.jpowsour.2014.02.012.

[4] J. Schmitt, A. Maheshwari, M. Heck, S. Lux, M. Vetter, Impedance change and capacity fade of lithium nickel manganese cobalt oxide-based batteries during calendar aging, J. Power Sources 353 (2017) 183–194, https://doi.org/10.1016/j.jpowsour.2017.03.090.

[5] B. Stiaszny, J.C. Ziegler, E.E. Krauß, M. Zhang, J.P. Schmidt, E. Ivers-Tiffée, Electrochemical characterization and post-mortem analysis of aged LiMn 2O4-NMC/graphite lithium ion batteries part II: calendar aging, J. Power Sources 258 (2014) 61–75, https://doi.org/10.1016/j.jpowsour.2014.02.019.

[6] M. Montaru, S. Fiette, J.L. Koné, Y. Bultel, Calendar ageing model of Li-ion battery combining physics-based and empirical approaches, J. Energy Storage 51 (2022), https://doi.org/10.1016/j.est.2022.104544.

[7] W. Li, J. Chen, K. Quade, D. Luder, J. Gong, D.U. Sauer, Battery degradation diagnosis with field data, impedance-based modeling and artificial intelligence, Energy Storage Mater. 53 (2022) 391–403, https://doi.org/10.1016/j.ensm.2022.08.021.

[8] W. Zhu, P. Zhou, D. Ren, M. Yang, X. Rui, C. Jin, T. Shen, X. Han, Y. Zheng, L. Lu, M. Ouyang, A mechanistic calendar aging model of lithium-ion battery considering solid electrolyte interface growth, Int. J. Energy Res. 46 (2022) 15521–15534, https://doi.org/10.1002/er.8249.

[9] K. Uddin, S. Perera, W.D. Widanage, L. Somerville, J. Marco, Characterising lithium-ion battery degradation through the identification and tracking of electrochemical battery model parameters, Batteries 2 (2016), https://doi.org/10.3390/batteries2020013.

[10] V. Ramadesigan, K. Chen, N.A. Burns, V. Boovaragavan, R.D. Braatz, V. R. Subramanian, Parameter estimation and capacity fade analysis of lithium-ion batteries using reformulated models, J. Electrochem. Soc. 158 (2011) A1048, https://doi.org/10.1149/1.3609926.

[11] L. Zhang, L. Wang, C. Lyu, J. Li, J. Zheng, Non-destructive analysis of degradation mechanisms in cycle-aged graphite/LiCoO2 batteries, Energies 7 (2014) 6282–6305, https://doi.org/10.3390/en7106282.

[12] G. Luo, Y. Zhang, A. Tang, Capacity degradation and aging mechanisms evolution of lithium-ion batteries under different operation conditions, Energies 16 (2023), https://doi.org/10.3390/en16104232.

[13] G. Sordi, M. Sedzik, A. Casalegno, C. Rabissi, Diagnosis of lithium-ion batteries degradation with P2D model parameters identification: a case study on low temperature charging, Review (n.d.).

[14] Sony Energy Devices Corporation, Lithium Ion Rechargeable Battery Technical Information Model US18650V3, 2011.

[15] C. Rabissi, G. Sordi, A. Innocenti, A. Casalegno, Fast and reliable calibration of thermal-physical model of lithium-ion battery: a sensitivity-based method, J. Energy Storage 59 (2023), https://doi.org/10.1016/j.est.2022.106435.
[16] J. Wang, J. Purewal, P. Liu, J. Hicks-Garner, S. Soukazian, E. Sherman, A. Sorenson, L. Vu, H. Tataria, M.W. Verbrugge, Degradation of lithium ion batteries employing graphite negatives and nickel-cobalt-manganese oxide + spinel manganese oxide positives: Part 1, aging mechanisms and life estimation, J. Power Sources 269 (2014) 937–948, https://doi.org/10.1016/j.jpowsour.2014.07.030.
[17] M.A. Rahman, S. Anwar, A. Izadian, Electrochemical model parameter identification of a lithium-ion battery using particle swarm optimization method, J. Power Sources 307 (2016) 86–97, https://doi.org/10.1016/j.jpowsour.2015.12.083.
[18] D. Lu, M. Scott Trimboli, G. Fan, Y. Wang, G.L. Plett, Nondestructive EIS testing to estimate a subset of physics-based-model parameter values for lithium-ion cells, J. Electrochem. Soc. 169 (2022) 080504, https://doi.org/10.1149/1945-7111/ac824a.
[19] C. Rabissi, A. Innocenti, G. Sordi, A. Casalegno, A comprehensive physical-based sensitivity analysis of the electrochemical impedance response of lithium-ion batteries, Energy Technol. 9 (2021), https://doi.org/10.1002/ente.202000986.
[20] P. Shafiei Sabet, A.J. Warnecke, F. Meier, H. Witzenhausen, E. Martinez-Laserna, D. U. Sauer, Non-invasive yet separate investigation of anode/cathode degradation of lithium-ion batteries (nickel–cobalt–manganese vs. graphite) due to accelerated aging, J. Power Sources 449 (2020), https://doi.org/10.1016/j.jpowsour.2019.227369.
[21] J. Wandt, A. Freiberg, R. Thomas, Y. Gorlin, A. Siebel, R. Jung, H.A. Gasteiger, M. Tromp, Transition metal dissolution and deposition in Li-ion batteries investigated by operando X-ray absorption spectroscopy, J Mater Chem A Mater 4 (2016) 18300–18305, https://doi.org/10.1039/C6TA08865A.
[22] S.J. An, J. Li, C. Daniel, D. Mohanty, S. Nagpure, D.L. Wood, The state of understanding of the lithium-ion-battery graphite solid electrolyte interphase (SEI) and its relationship to formation cycling, Carbon N Y 105 (2016) 52–76, https://doi.org/10.1016/j.carbon.2016.04.008.
[23] J.S. Edge, S. O'Kane, R. Prosser, N.D. Kirkaldy, A.N. Patel, A. Hales, A. Ghosh, W. Ai, J. Chen, J. Yang, S. Li, M.C. Pang, L. Bravo Diaz, A. Tomaszewska, M. W. Marzook, K.N. Radhakrishnan, H. Wang, Y. Patel, B. Wu, G.J. Offer, Lithium ion battery degradation: what you need to know, Phys. Chem. Chem. Phys. 23 (2021) 8200–8221, https://doi.org/10.1039/d1cp00359c.
[24] C.R. Birkl, M.R. Roberts, E. McTurk, P.G. Bruce, D.A. Howey, Degradation diagnostics for lithium ion cells, J. Power Sources 341 (2017) 373–386, https://doi.org/10.1016/j.jpowsour.2016.12.011.
[25] S. Schindler, M.A. Danzer, A novel mechanistic modeling framework for analysis of electrode balancing and degradation modes in commercial lithium-ion cells, J. Power Sources 343 (2017) 226–236, https://doi.org/10.1016/j.jpowsour.2017.01.026.
[26] M. Dubarry, C. Truchot, B.Y. Liaw, Synthesize battery degradation modes via a diagnostic and prognostic model, J. Power Sources 219 (2012) 204–216, https://doi.org/10.1016/j.jpowsour.2012.07.016.
[27] A. Maheshwari, M. Heck, M. Santarelli, Cycle aging studies of lithium nickel manganese cobalt oxide-based batteries using electrochemical impedance spectroscopy, Electrochim. Acta 273 (2018) 335–348, https://doi.org/10.1016/j.electacta.2018.04.045.

List of acronyms

Acronym	Description
BOL:	Begin of life
CC:	Constant current
CV:	Constant Voltage
DMC:	Dimethyl carbonate
DV:	Differential Voltage
ECM:	Equivalent Circuit Model
EDS:	Energy Dispersive X-ray Spectroscopy
EIS:	Electrochemical Impedance Spectroscopy
HFR:	High-Frequency Resistance
LAM:	Loss of Active electrode Material
LFP:	Lithium-iron-phosphate battery
LLI:	Loss of Lithium Inventory
LMO:	Lithium-manganese-oxide battery
NMC:	Lithium-nickel-manganese-cobalt-oxide battery
OCP:	Open-Circuit Potential
OCV:	Open-Circuit Voltage
P2D:	Pseudo-two dimensional
PSO:	Particle Swarm Optimisation
RMSE:	Root-Mean Squared Error
SEI:	Solid electrolyte interphase
SEM:	Scanning Electron Microscope
SoC:	State of charge